A stochastic volume approach based on tailored Green's functions for airfoil noise prediction at low Mach number

Nicolas Trafny, Gilles Serre, Benjamin Cotté, Jean-François Mercier

A stochastic volume approach based on tailored Green's functions for airfoil noise prediction at low Mach number

N. Trafny[a,b], G. Serre[a], B. Cotté[b], J-F. Mercier[c]

[a] *Naval Group, Naval Research, Ollioules, France*
[b] *IMSIA, ENSTA Paris, CNRS, CEA, EDF, Institut Polytechnique de Paris*
[c] *POEMS, ENSTA Paris, CNRS, INRIA, Institut Polytechnique de Paris*

Abstract

The presence of boundary surfaces in a turbulent flow can result in the enhancement of the radiated acoustic field especially for eddies close to any geometrical singularity. At low Mach number, the best suited prediction methods consist in using an acoustic analogy solved with an integral formulation. In the present study, we focus on the Lighthill's wave equation combined with a tailored Green's function and a new semi-analytical model for the turbulence statistics in the space-frequency domain to extend acoustic analogies to geometries of arbitrary shapes. To validate the model predictions for the leading edge noise and the trailing edge noise, a NACA 0012 airfoil at zero angle of attack is considered and predictions are compared to experimental data. The volume integral approach introduced in this study allows us to study the spatial distribution of the noise sources inside the turbulence volume. In addition, the direct noise radiation associated with the turbulent boundary layer is investigated.

Keywords: Green's function, Underwater noise, Lighthill analogy, Semi-analytical turbulence model, Leading edge noise, Trailing edge noise, Monte Carlo quadrature methods, Boundary layer noise

1. Introduction

The interaction between a turbulent flow and a rigid boundary surface leads to an acoustic radiation of broadband nature whose characterization is of inter-

est in many industrial applications. Because industrial underwater propellers operate at low Mach numbers and high Reynolds numbers, techniques based on compressible Direct Numerical Simulations (DNS) or Large Eddy Simulations (LES) are too expensive. Also, there are few experimental data available so empirical methods might not be reliable in an industrial context. The most suitable alternative appears to be the use of an acoustic analogy. It consists in the separation between noise generation and noise propagation. This idea was initially proposed by Lighthill [1] and applied to jet noise. Since then, his work has been extended by Curle [2] in order to take into account the effect of a rigid boundary placed in the flow. However, it has been shown that the knowledge of the compressible part of the flow is mandatory to apply Curle's analogy to a non-compact geometry [3, 4]. At low Mach number, it becomes an issue because the cost of a compressible flow simulation is prohibitive as it is proportional to Re^3/M^4 for a compressible DNS and to Re^2/M^4 for a compressible LES [5]. Thus, we are forced to use an incompressible approximation of the flow limiting the classical Curle's analogy to low frequencies.

Two strategies based on the Green functions formalism can be distinguished to overpass this limitation. The first one, proposed by Schram [6], consists in combining Curle's analogy with a boundary element method in order to compute the acoustic pressure over the surface in a first step and then to compute the radiated pressure. The second strategy consists in using a tailored Green's function that takes into account the diffraction effects that are lacking in an incompressible flow model. By definition, a tailored Green function satisfies the Neumann boundary condition at the boundary surfaces : it is known analytically for canonical geometries or can be computed numerically for arbitrary shapes. Tailored Green's functions have been mostly used for dimensional analysis [7, 8]. More recently, tailored Green's functions have been applied to roughness noise [9]. However, existing practical applications based on a tailored Green function either are restricted to wall pressure spectrum prediction [10], when the geometry is assimilated to an infinite plate, or need a time-accurate description of the turbulent flow [11], which we want to avoid for engineering applications

because of prohibitive costs.

In the present study, we propose an approach based on a tailored Green's function combined to an analytical model for the turbulent flow statistics that allow us to consider realistic geometries. As a first step, we focus on edge noise prediction due to the interaction of inflow turbulence with the airfoil leading edge or the turbulent fluctuations in the boundary layer with the airfoil trailing edge. Over the last decades, the trailing edge noise mechanism has been widely investigated [12] through the theory of Amiet [13] or the diffraction theory [14, 15] and robust experimental data are available in air. In these theories, it is assumed that an airfoil can be well approximated by a semi-infinite plate to account for the edge diffraction and the computation of the radiated noise requires the knowledge of the wall pressure spectrum [16]. These theories assume that the wall pressure field must be statistically homogeneous [17], and that the wall pressure spectrum must be evaluated at some distance upstream of the trailing edge. The choice for this distance is arbitrary: Lee et al. [18] use the boundary layer parameters at 97.5% of the chord, Stalnov et al. [19] use 97.8% and the parameters are extracted at 99% of the chord in the BANC III benchmark [20]. If the turbulent boundary layer is not homogeneous in the streamwise direction close to the trailing edge, the predicted levels are somewhat sensitive to the location where the wall pressure spectrum is calculated. Also, the spatial extent of the turbulence volume is assumed infinite in the streamwise direction so the history of the boundary layer is not taken into account in theses theories. Since existing models of the two-point statistics of the turbulent velocity have been developed for these theories, they are expressed in the wavenumber-frequency space making them unsuitable for curved geometries of finite extent. It appears that a new analytical model for the two-point statistics of the turbulent velocity expressed in the physical space is mandatory to consider the evolution of the boundary layer in the streamwise direction. Therefore this paper has three objectives: 1-to justify the feasibility of a global approach based on both a tailored Green function and a statistical description of the turbulence, 2-to present a new analytical model for the two-point statistics of the

turbulent velocity in the physical space and 3-to investigate the accuracy of the predictions obtained with the developed global approach.

This paper is organized as follow. In Section 2, we reproduce the derivation of Lighthill's analogy based on the free-field Green's function or on a tailored Green's function, satisfying a Neumann boundary condition, and we introduce the Monte Carlo quadrature method that we use to evaluate the 6-dimensional integral. In Section 3, we derive a new expression for the turbulent velocity cross-spectrum expressed in the physical space and in the frequency domain. In Section 4, we compare the trailing edge and leading edge noise model predictions to experimental data, and we confront the boundary layer noise model to empirical models from the literature.

2. The Lighthill acoustic analogy

2.1. Evaluation of the far field radiated noise

In the frequency domain, the fundamental equation governing the generation of sound in the presence of rigid boundaries at low Mach number is [21]:

$$p(\mathbf{x},\omega) = \int_V \frac{\partial^2 \mathrm{G}(\mathbf{x},\mathbf{y},\omega)}{\partial y_i \partial y_j} T_{ij}(\mathbf{y},\omega) dV(\mathbf{y}) + \oint_S p_{ij}(\mathbf{y},\omega) \frac{\partial \mathrm{G}(\mathbf{x},\mathbf{y},\omega)}{\partial y_i} n_j(\mathbf{y}) dS(\mathbf{y}), \tag{1}$$

where p is the pressure fluctuation, V is the turbulence volume surrounding a solid boundary S, $\mathbf{n}$ is the unit normal that points into the fluid, T_{ij} is the Lighthill stress tensor, $\mathbf{x}$ is the observer location, p_{ij} is the compressive stress tensor, ω is the angular frequency and where G is the Green function. The Green function is the causal solution at $\mathbf{x} = (x_1, x_2, x_3)$ of the wave equation generated by an impulsive point source at $\mathbf{y} = (y_1, y_2, y_3)$ and is defined by:

$$(\nabla^2 + k_0^2)\mathrm{G}(\mathbf{x},\mathbf{y},\omega) = \delta(\mathbf{x}-\mathbf{y}), \tag{2}$$

where $k_0 = \omega/c_0$ is the acoustic wavenumber with c_0 the sound speed. There are an infinite number of Green's functions, but it is often convenient either to use the free-field Green function G_0 or the tailored Green function G_T that

satisfies the rigid wall boundary condition on S:

$$\frac{\partial \mathrm{G}_T(\mathbf{x},\mathbf{y},\omega)}{\partial y_i} n_i(\mathbf{y}) = 0, \quad \forall \mathbf{y} \in S. \tag{3}$$

Then, two classes of prediction models for broadband flow-induced noise can be formulated:

$$p(\mathbf{x},\omega) = \int_V \frac{\partial^2 \mathrm{G}_0(\mathbf{x},\mathbf{y},\omega)}{\partial y_i \partial y_j} T_{ij}(\mathbf{y},\omega) dV(\mathbf{y}) + \oint_S p_{ij}(\mathbf{y},\omega) \frac{\partial \mathrm{G}_0(\mathbf{x},\mathbf{y},\omega)}{\partial y_i} n_j(\mathbf{y}) dS(\mathbf{y}), \tag{4}$$

which is the Curle's equation, and

$$p(\mathbf{x},\omega) = \int_V \frac{\partial^2 \mathrm{G}_T(\mathbf{x},\mathbf{y},\omega)}{\partial y_i \partial y_j} T_{ij}(\mathbf{y},\omega) dV(\mathbf{y}). \tag{5}$$

By introducing $\mathrm{G}_S = \mathrm{G}_T - \mathrm{G}_0$, the total field p can be defined as the sum of a direct field p_d of quadrupolar nature and a scattered field p_s, which takes into account the presence of the rigid boundaries. Therefore, the direct field :

$$p_d(\mathbf{x},\omega) = \int_V \frac{\partial^2 \mathrm{G}_0(\mathbf{x},\mathbf{y},\omega)}{\partial y_i \partial y_j} T_{ij}(\mathbf{y},\omega) dV(\mathbf{y}), \tag{6}$$

can be distinguished from the scattered field:

$$p_s(\mathbf{x},\omega) = \oint_S p_{ij}(\mathbf{y},\omega) \frac{\partial \mathrm{G}_0(\mathbf{x},\mathbf{y},\omega)}{\partial y_i} n_j(\mathbf{y}) dS(\mathbf{y}) = \int_V \frac{\partial^2 \mathrm{G}_S(\mathbf{x},\mathbf{y},\omega)}{\partial y_i \partial y_j} T_{ij}(\mathbf{y},\omega) dV(\mathbf{y}). \tag{7}$$

As already shown by Gloerfelt et al. [22], Eqs. (4) and (5) are equivalent but Eq. (4) is more complicated as it requires a good approximation of p_{ij} over the surface. To compute the radiated noise for a non-compact surface using the free field Green function, p_{ij} must indeed be known and in particular its acoustic component [3], otherwise the radiated pressure levels are highly overestimated. The most direct way to compute it is during the calculation of the source term by using a compressible simulation of the flow. As already discussed, this is very difficult to be achieved at low Mach and high Reynolds numbers. An alternative consists in using an incompressible flow simulation with a boundary element method to compute the acoustic pressure fluctuations over the surface first, then to compute Eq. (4) [23]. This limitation can also be overpassed by using a tailored Green function that contains all the diffraction effects due to the

presence of the rigid boundary surfaces inside the turbulent flow. The difficulty due to the calculation of the compressible component of p_{ij} on the surface is then transferred to the calculation of the tailored Green function. Looking at Eq. (5), it appears that the second derivatives of the tailored Green function define the flow noise production. The main advantage of this alternative approach comes from the fact that the tailored Green function can be computed independently of the source and thus of the flow. It can therefore be used to investigate the ability of a given geometry to radiate noise efficiently, to calculate the directivity of the radiated noise and to identify the turbulent flow regions that will most effectively contribute, as denoted by Ffowcs Williams [24]. Tailored Green's functions are only known analytically for simple geometries but they can be computed numerically using the boundary element method [9] for boundaries of arbitrary shapes. Although the present study is restricted to geometries leading analytical Green functions, all the developments are made with the concern to be straightforwardly applicable to arbitrary geometries.

At this point, the source term $T_{ij} \approx \rho_0 u_i u_j$, with u_i the flow velocity, still has to be modelled. The most direct methods are based on a time-accurate simulation of the turbulent flow. However and as already pointed out, these methods are too expensive for high Reynolds numbers flows. On the one hand, at high frequencies the radiated noise is produced by small eddies that require a very fine grid to be modelled. On the other hand, the spatial extent of the computational domain must be larger than the turbulent flow correlation length scales that can be very large at low frequency [25]. Rather than using a time-accurate description of the turbulent flow, stochastic noise generation and radiation (SNGR) methods can be used. These approaches have been successfully applied to trailing edge noise prediction [26] but very large computer resources are required in order to generate and store turbulence description data. Finally, a statistical description of the turbulent flow can be employed. The main avantage of this alternative is that a statistical model can be built without the knowledge of the instantaneous turbulent flow variables. For instance, a simulation of the mean flow or an estimate of the turbulent boundary layer parameters can be

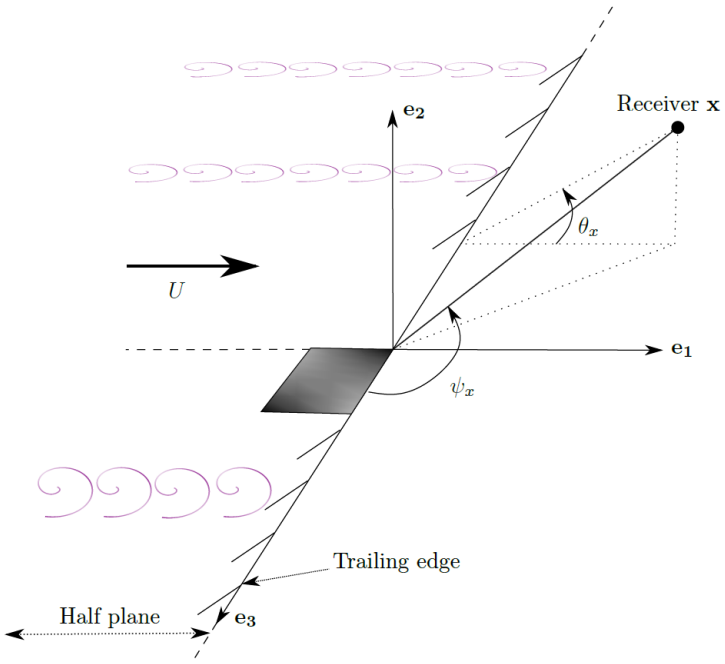

Figure 1: Coordinate system and semi-infinite plate definition for trailing edge noise prediction

used to compute the turbulent velocity cross-correlation functions required in the flow noise prediction model. Moreover, a statistical model can be expressed directly in the frequency domain making it the most suitable approach for a noise prediction model based on the Green's function formalism.

2.2. Sound generation by a turbulent flow in the vicinity of a scattering half plane

In the scope of edge noise prediction models, the foil is usually assimilated to an infinite half-plane. For trailing edge noise, we focus on the noise radiated by a turbulent boundary layer of finite dimensions scattered at the edge of this half-plane. Referring to Fig. 1, we consider here that a turbulent boundary layer with transverse mean shear is developing over the plate. For leading edge noise, we assume that the foil is immersed in an homogeneous incident turbulent flow. In both cases, only the streamwise component of the mean velocity is non-zero: in the boundary layer, the mean velocity $\mathbf{U} = U_1(y_2)\mathbf{e}_1$ is only a function of

the distance to the wall and it is a constant for an inflow turbulence without mean shear. Assuming an incompressible flow and considering only the mean-shear/turbulence interaction term [27], Eq. (5) becomes:

$$p(\mathbf{x},\omega) = \int_V 2\rho_0 U_1(y_2) \left(\frac{\partial^2 \mathrm{G}_T(\mathbf{x},\mathbf{y},\omega)}{\partial y_1^2} u_1'(\mathbf{y},\omega) + \frac{\partial^2 \mathrm{G}_T(\mathbf{x},\mathbf{y},\omega)}{\partial y_1 \partial y_2} u_2'(\mathbf{y},\omega) + \frac{\partial^2 \mathrm{G}_T(\mathbf{x},\mathbf{y},\omega)}{\partial y_1 \partial y_3} u_3'(\mathbf{y},\omega) \right) dV(\mathbf{y}), \tag{8}$$

where u_i' denotes the velocity fluctuations defined by $u_i = U_i + u_i'$. The power spectral density is then expressed by :

$$\begin{aligned} S_{pp}(\mathbf{x},\omega) &= \langle p(\mathbf{x},\omega) p^*(\mathbf{x},\omega) \rangle \\ &= \int_V \int_V 4\rho_0^2 U_1(y_2) U_1(z_2) \left(\phi_{ij}(\mathbf{y},\mathbf{z},\omega) \frac{\partial^2 \mathrm{G}_T(\mathbf{x},\mathbf{y},\omega)}{\partial y_1 \partial y_i} \frac{\partial^2 \mathrm{G}_T^*(\mathbf{x},\mathbf{z},\omega)}{\partial z_1 \partial z_j} \right) dV(\mathbf{y}) dV(\mathbf{z}) \end{aligned} \tag{9}$$

where $\phi_{ij}(\mathbf{y},\mathbf{z},\omega) = \langle u_i(\mathbf{y},\omega) u_j^*(\mathbf{z},\omega) \rangle$ are the turbulent velocity cross-correlation spectra, $\langle\rangle$ is the ensemble average operator and the superscript $*$ denotes the complex conjugate. $\mathbf{y}$ and $\mathbf{z}$ are two sources position inside the turbulence volume V. Therefore, the computation of Eq. (9) requires the knowledge of all the velocity fluctuation spectra ϕ_{ij} expressed in the physical space which will be studied in Section 3. The expressions for the Green's function tailored to a semi-infinite plate are presented in Appendix A.

2.3. Monte Carlo integration methods

In order to evaluate the power spectral density using Eq. (9), a 6-dimensional integration must be performed. The most suitable type of methods for evaluating integrals with a large number of dimensions are those based on stochastic techniques: Monte Carlo methods. While the error made by deterministic quadrature methods increases exponentially with the number of dimensions, the one associated with probabilistic method simply does not depend on it. It can be shown that the error decreases in the worst case (i.e. without using any adaptative method) as $N^{-1/2}$, where N is the number of samples of the integrand function [28]. The counterpart of Monte Carlo integration methods is that a high integration precision cannot be achieved. But a high precision is

not necessary since a targeted ±1 dB precision on the radiated sound pressure level is reached for a relative error on the pressure spectrum of 25%. There are several adaptative methods used to reduce the integration error [29] and the most popular ones are importance sampling and stratified sampling. On the one hand, the idea of importance sampling is to modify the probability density function, which is uniform in the classical Monte Carlo integration method, in order to concentrate the integrand evaluations points in the regions of largest magnitude. On the other hand, the stratified sampling technique consists in the subdivision of the integration domain into sub-domains over which the integral will be evaluated.

The GNU Scientific Library (GSL) implements the VEGAS [29] algorithm which makes use of both importance and stratified sampling techniques. It is an iterative algorithm that constantly adapts to the integrand until a chosen convergence criteria is reached. Moreover, it allows us to estimate the consistency of the computed integration error by computing the Chi-square χ^2 by degree of freedom. According to the GSL documentation, a good choice of the convergence criterion on the χ^2 is to set it to 0.5. At each iteration, the integrand is evaluated $N_i = 10^5$ times. The computation ends when both a precision of 25% and the convergence criteria are reached. It appears that the number of integrand evaluations made at each iteration could have a significant impact on the convergence of the quadrature algorithm especially at high frequency, when this number should be increased.

3. Statistical description of the turbulent flow

3.1. Turbulent velocity cross-spectrum in physical space

Once the tailored Green's function is known, the remaining term that is required for the computation of the power spectral density using Eq. (9) is the turbulent velocity cross-correlation spectrum ϕ_{ij}. In order to derive an analytical expression for ϕ_{ij}, we assume in the first place an homogeneous and isotropic turbulent flow. The wavenumber spectrum of the velocity fluctuations

can be expressed in a frame of reference moving with the average flow as [30]:

$$\widetilde{\phi}_{ij}^{(1,2,3)}(k_1,k_2,k_3) = \frac{E(k)}{4\pi k^2}\left(\delta_{ij} - \frac{k_i k_j}{k^2}\right), \tag{10}$$

where $E(k)$ is the turbulent kinetic energy spectrum and $k = \sqrt{k_1^2 + k_2^2 + k_3^2}$ is the wavenumber magnitude. There are several ways to express $E(k)$ but the most widely used model is the one suggested by von Kármán :

$$E(k) = \frac{55}{9\sqrt{\pi}}\frac{\Gamma(5/6)}{\Gamma(1/3)}\frac{\overline{u^2}}{k_e}\frac{(k/k_e)^4}{[1+(k/k_e)^2]^{17/6}}, \tag{11}$$

with k_e the energy bearing wavenumber and $\overline{u^2}$ the variance of the turbulence fluctuations, identical in any direction for an isotropic turbulence ($\overline{u^2} = \overline{u_1^2} = \overline{u_2^2} = \overline{u_3^2}$). Still for isotropic turbulence, the wavenumber k_e can be defined in terms of the longitudinal integral length scale $L_{11}^{(1)}$:

$$k_e = \frac{\sqrt{\pi}}{L_{11}^{(1)}}\frac{\Gamma(5/6)}{\Gamma(1/3)}. \tag{12}$$

The wavenumber spectrum of the velocity fluctuations can be expressed in the fixed frame of reference by introducing the convection mean velocity U_c and the moving axis spectrum $\phi_m(\omega - U_c k_1)$:

$$\widetilde{\phi_{ij}}(k_1,k_2,k_3,\omega) = \widetilde{\phi_{ij}}^{(1,2,3)}(k_1,k_2,k_3)\phi_m(\omega - U_c k_1). \tag{13}$$

Then, following Blake [30], the classical frozen turbulence assumption is modified in order to take into account the moving-axis decay. He suggested to describe this decay using:

$$\phi_m(\omega - U_c k_1) = \delta(\omega - U_c k_1)\mathrm{e}^{-\gamma|\omega r_1/U_c|}, \tag{14}$$

where $\gamma = 0.3$ is an empirical parameter and where $\mathbf{r} = \mathbf{y} - \mathbf{z} = (r_1, r_2, r_3)$ is the correlation distance. The velocity cross-correlation spectra is then obtained by taking the inverse Fourier transform of (13). It yields:

$$\phi_{ij}(r_1,r_2,r_3,\omega) = \mathrm{e}^{-\gamma|\omega r_1/U_c|}\frac{\mathrm{e}^{\mathrm{i}\omega r_1/U_c}}{U_c}\iint_{-\infty}^{\infty}\widetilde{\phi_{ij}}^{(1,2,3)}(\omega/U_c,k_2,k_3)\mathrm{e}^{\mathrm{i}(k_2 r_2 + k_3 r_3)}dk_2 dk_3. \tag{15}$$

Then, it is shown in Appendix C that the turbulence velocity cross-correlation spectrum can be written as:

$$\phi_{ij}(r_1, r_2, r_3, \omega) = \frac{55}{9\sqrt{\pi}} \frac{\Gamma(5/6)}{\Gamma(1/3)} \frac{\overline{u^2}}{4\pi k_e} \mathrm{e}^{-\gamma|\omega r_1/U_c|} \frac{\mathrm{e}^{\mathrm{i}\omega r_1/U_c}}{U_c} \varphi_{ij}(\xi_2, \xi_3, \omega), \qquad (16)$$

where $\xi_i = k_e r_i$. The expressions of the φ_{ij} are detailed in Appendix C.

3.2. Estimates of the turbulent parameters

To compute ϕ_{ij} with Eq. (16) we have to define : the energy bearing wavenumber k_e, the convection mean velocity U_c and the variance of the turbulent fluctuations $\overline{u^2}$. For leading edge noise calculations, if we assume an homogeneous and isotropic inflow turbulence, both k_e and $\overline{u^2}$ are constants and they are obtained straightforwardly from an experimental estimate of the longitudinal integral length scale and the turbulence intensity. U_c is also constant and equal to the inlet mean velocity. For trailing edge noise prediction, or if the incident turbulence is non-homogeneous, there are many strategies, depending on how the turbulent flow is simulated. We have chosen to define k_e, U_c and $\overline{u^2}$ from a calculation of the boundary layer parameters along the airfoil chord. Since a turbulent boundary layer cannot be reasonably assumed homogeneous, we will have to introduce an inhomogeneity in the model. This can be achieved by assuming that k_e, U_c and $\overline{u^2}$ depend on the source location. In the present study, all parameters of the turbulent boundary layer are estimated from an XFoil simulation. The XFoil [31] prediction code provides an estimate of the boundary layer quantities along the chord of the profile such as the boundary layer displacement thickness δ^* and momentum thickness θ, the friction coefficient C_f, the pressure coefficient C_p and the velocity at the edge of the boundary layer U_e. The calculation of the turbulent parameters from an estimation of the boundary layer parameters is presented in Appendix B.

4. Results

In order to validate the model predictions for both trailing edge noise and leading edge noise, a NACA 0012 airfoil at zero angle of attack is considered.

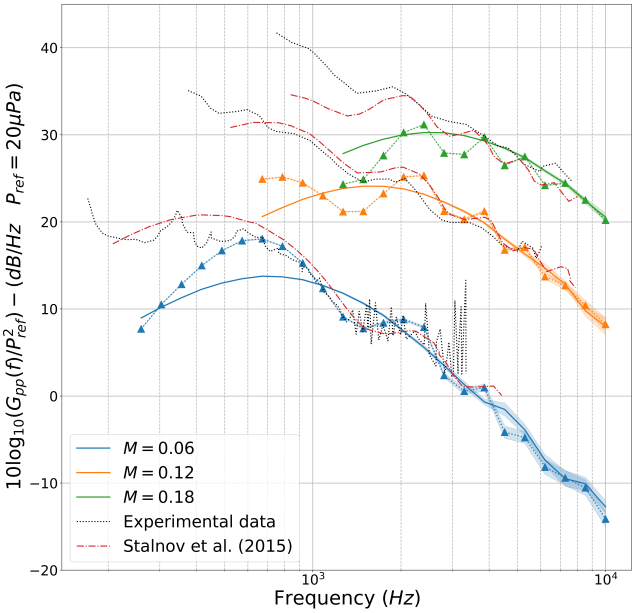

Figure 2: Acoustic pressure spectrum ($G_{pp}(f) = 4\pi S_{pp}(\omega)$) for an observer at $1.17m$ above the trailing edge obtained for three Mach numbers M using Eq. (9) and (———) the compact source approximation of the Green function (A.3) or (····▲····) the multiple scattering Green function (A.4). Transparent areas define the estimated integration error given by the VEGAS algorithm.

For comparison purpose, we use the experimental data of [19] for trailing edge noise and [32] for leading edge noise. Then, the model predictions for boundary layer noise are compared with empirical models from the literature. Finally, a method to reduce computational costs is introduced. For each spectrum, estimated integration errors associated with the Monte Carlo quadrature methods described in Section 2.3, are plotted and denoted by transparent areas.

4.1. Trailing edge noise prediction

First, we focus on trailing edge noise prediction for a NACA 0012 profile of chord $c = 0.2$ m and span $L = 0.45$ m. Figure 2 shows the far-field radiated

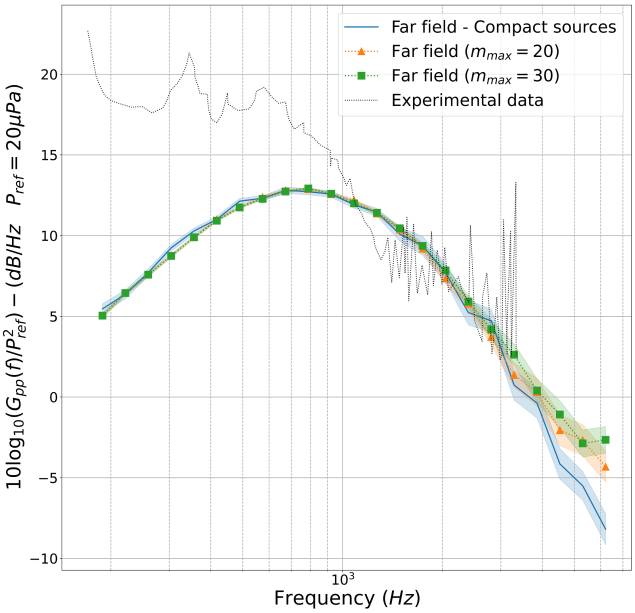

Figure 3: Acoustic pressure spectrum ($G_{pp}(f) = 4\pi S_{pp}(\omega)$) for an observer at $1.17m$ above the trailing edge obtained for $M = 0.06$ using Eq. (9) and the compact source approximation of the Green function (A.3) or the far field approximation (A.2). Transparent areas define the estimated integration error given by the VEGAS algorithm.

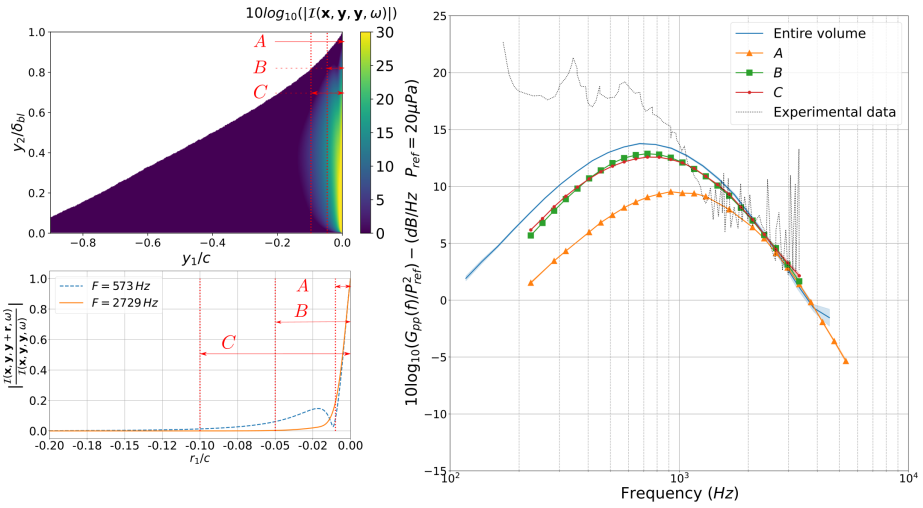

Figure 4: (*Right*) Acoustic pressure spectrum ($G_{pp}(f) = 4\pi S_{pp}(\omega)$) for an observer at $1.17m$ above the trailing edge obtained using Eq. (9) and the far field approximation of the Green function (Eq. (A.2) with $m_{max} = 20$). Study of the contribution of three regions of the turbulence volume, far from the edge, which extend from $y_1/c = 0$ to: $y_1/c = -0.01$ (A), $y_1/c = -0.05$ (B) and $y_1/c = -0.1$ (C). (*Left*) Absolute value of the integrand (Eq. (17)) in the turbulent boundary layer evaluated at 573 Hz and for $\mathbf{y} = \mathbf{z}$ (*Top*) - Normalized absolute value of the integrand for a source above the trailing edge at $\mathbf{y} = (0, \delta_{bl}/2, 0)$ and $\mathbf{z} = \mathbf{y} + r_1\mathbf{e_1}$(*Bottom*).

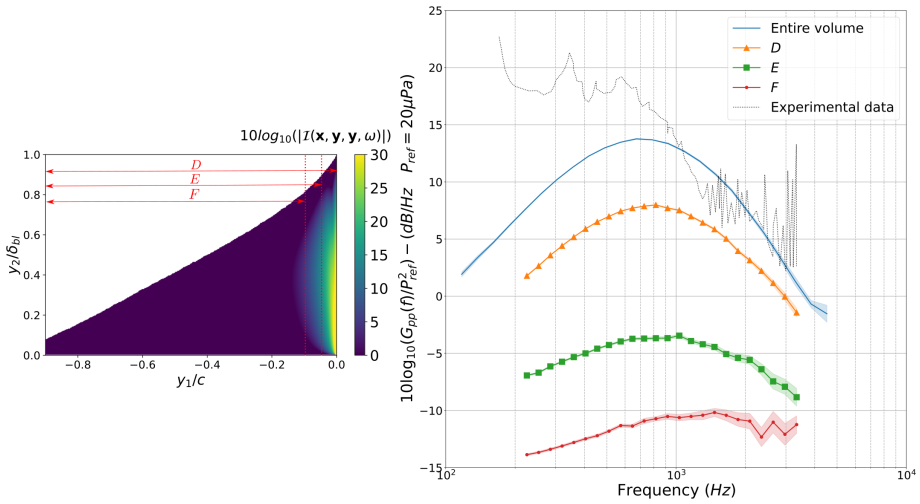

Figure 5: (*Right*) Acoustic pressure spectrum ($G_{pp}(f) = 4\pi S_{pp}(\omega)$) for an observer at $1.17m$ above the trailing edge obtained using Eq. (9) and the far field approximation of the Green function (Eq. (A.2) with $m_{max} = 20$). Study of the contribution of three regions of the turbulence volume, far from the edge, which extend from $y_1/c = -1.0$ to: $y_1/c = -0.01$ (D), $y_1/c = -0.05$ (E) and $y_1/c = -0.1$ (F). (*Left*) Absolute value of the integrand (Eq. (17)) in the turbulent boundary layer at 573 Hz and for $\mathbf{y} = \mathbf{z}$.

noise spectrum predictions obtained using the compact approximation (A.3) of the Green function and the Multiple Scattering Green function (A.4) for a zero angle of attack and at various Mach numbers. Three wind speeds are chosen : 20.58 m.s^{-1}, 41.16 m.s^{-1} and 61.74 m.s^{-1}. The observer is located at $1.17m$ above the trailing edge and at mid-span. The airfoil model was tripped using a roughness strip on both sides to ensure a fully developed turbulent boundary layer. In the XFoil simulation, the laminar to turbulent transition is forced at the leading edge. At low frequencies significant differences can be observed. As explained by Stalnov et al. [19], the increase of the measurement is due to the jet noise in the wind tunnel and is not accounted for by our prediction model. At higher frequencies, both trends and absolute levels are in good agreement with experimental data. Oscillations due to the non-compactness of the airfoil are well predicted by the Multiple Scattering Green function, especially at $M = 0.06$. The predicted maximum peaks appear to be well localized which means that the integral length scales are also correctly predicted.

To confirm that the use of the compact approximation (A.3) of the Green's function is sufficient, Figure 3 shows the predictions obtained at $M = 0.06$ with the far-field approximation of the Green function (Eq. (A.2)) and calculated for two values of m_{max}, the number of terms in the truncated series. It appears that the use of the compact approximation is perfectly justified up to at least 4 kHz. Beyond that, a discrepancy between the results obtained with the two Green functions appears and it reaches about 3 dB at 6 kHz, in a frequency range where the comparison with the experimental results is unfortunately not available. This result confirms what we observed on the calculation of the second derivatives of Green's function (see Figure A.12): the sources close to the edge contribute most effectively to the global radiation.

We can study more quantitatively this particularity, thanks to an advantage of the volume integral approach over the surface integral approaches: its ability to study the contribution of different regions of the turbulent volume to the radiated noise. In order to do that, we present the contributions of 6 different regions in the boundary layer in Figures 4 and 5. The turbulence volume is

truncated at three points: $y_1/c = -0.01$, $y_1/c = -0.05$ and $y_1/c = -0.1$. The regions denoted as A, B and C are defined on Figure 4 and correspond to the areas closest to the trailing edge. The regions denoted as D, E and F are defined on Figure 5 and correspond to the most distant ones. Here, the far-field approximation of the Green's function tailored to the semi-infinite plane (Eq. (A.2) with $m_{max} = 20$) must be used because the compact approximation (Eq. (A.3)) would not allow us to correctly quantify the contributions of the sources far from the trailing edge. On the left side of Figures 4 and 5 is plotted the spatial evolution of the absolute value of the integrand in Eq. (9), i.e :

$$|\mathcal{I}(\mathbf{x},\mathbf{y},\mathbf{z},\omega)| = \left| 4\rho_0^2 U_1(y_2) U_1(z_2) \phi_{ij}(\mathbf{y},\mathbf{z},\omega) \frac{\partial^2 \mathrm{G}_T}{\partial y_1 \partial y_i}(\mathbf{x},\mathbf{y},\omega) \frac{\partial^2 \mathrm{G}_T^*}{\partial z_1 \partial z_j}(\mathbf{x},\mathbf{z},\omega) \right|. \tag{17}$$

Contrary to what was observed on the second derivatives of the Green's function (see Figure A.12), the sources that contribute most efficiently to the radiated noise are not the ones closest to the edge, but those located above the trailing edge. This is obviously explained by the fact that $U_1 = 0$ on the airfoil surface ($y_2 = 0$). Thus, the integrand cancels on the wall and the contribution of the viscous sublayer to the overall radiated noise turns out to be negligible, as can be seen in Figure 4. On Figure 4 (*right*), it appears that considering only the 5% closest to the edge (area B) allows to obtain a satisfactory estimate of the radiated noise and that the contribution of the rest of the volume is negligible on the whole frequency range. However, considering the 1% closest to the edge yields to a significant underestimation of the acoustic pressure spectrum for frequencies below 2kHz. On Figure 4 (*bottom-left*), we plot the normalized integrand Eq. (17) for $\mathbf{y} = (0, \delta_{bl}/2, 0)$ and $\mathbf{z} = \mathbf{y} + r_1\mathbf{e_1}$ and for a correlation distance in the streamwise direction varying from $r_1 = -0.2c$ to $r_1 = 0$. At 573 Hz, it can be observed that if the boundary layer is truncated at 1% of the chord (area A) a significant part of the integrand is neglected which yields to the underestimated pressure levels observed on the radiated pressure spectrum. At low frequency, a deviation up to 2dB can be observed between the contributions of areas (B) and (C) and the result obtained with the entire volume.

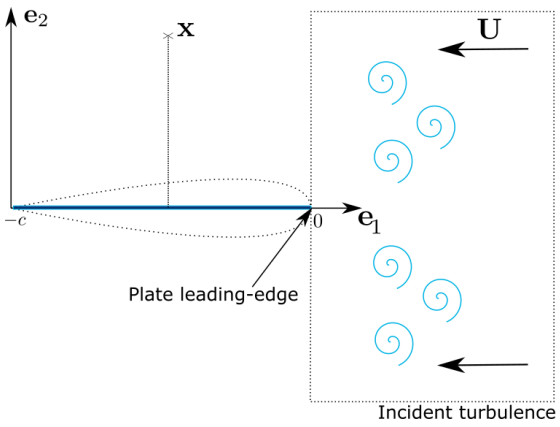

Figure 6: Illustration of the leading-edge noise configuration

These differences can be explained by the fact that by truncating the volume of turbulence, the effects of cross-correlations between vortices close to the edge and those far from the edge are neglected. The conclusion of Fig. 4 is that by judiciously truncating the turbulence volume, it is then possible to take advantage of a reduction in computation time with a small impact on the quality of the predictions. Finally, the contributions of the regions far from the edge are studied in Figure 5. The frequency slopes associated with regions E and F are significantly different from those associated with the other regions (A, B and C). Looking at the region F, it appears that the frequency slope tends to become a constant and the "bell" shape of the spectrum has disappeared.

4.2. Leading edge noise prediction

For leading edge noise prediction, we consider a NACA 0012 airfoil, of chord $c = 0.23$ m and span $L = 0.53$ m immersed in a free-stream turbulence of constant integral length scale. The configuration is presented in Figure 6. We assume that there is no turbulent boundary layer over the airfoil surface so that only leading edge noise is calculated. According to Paterson and Amiet [32], the longitudinal integral length scale is taken equal to $L_{11}^{(1)} = 0.3\,\mathrm{m}$ and the turbulence intensity to $I = 4.5\%$. Since only eddies close to the edge have a significant contribution to the total radiated noise levels, the size of

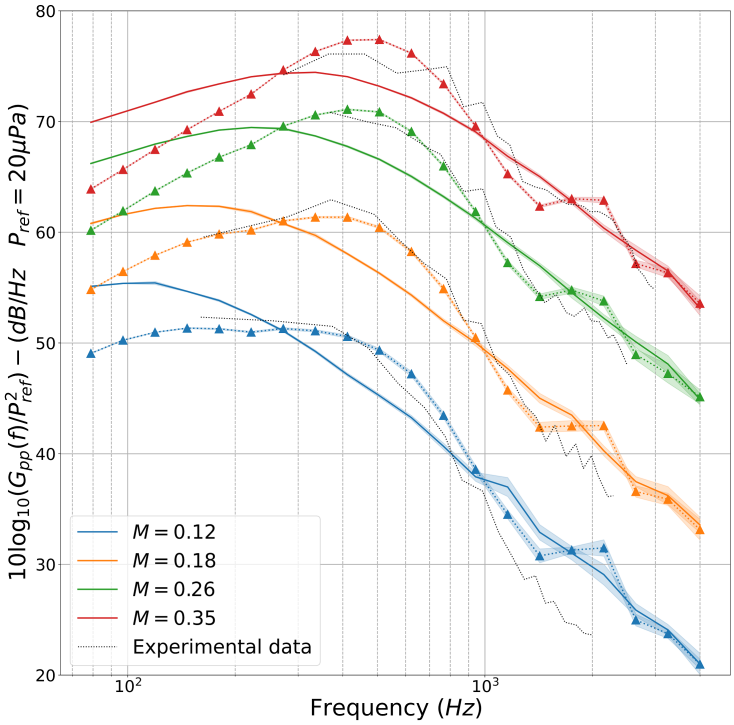

Figure 7: Acoustic pressure spectrum ($G_{pp}(f) = 4\pi S_{pp}(\omega)$) for leading edge noise at an observer at $2.25m$ and at mid-chord above the profile, obtained using Eq. (9) and (———) the compact source approximation of the Green function (A.3) or (····▲····) the multiple scattering Green function (A.4). Transparent areas define the estimated integration error given by the VEGAS algorithm.

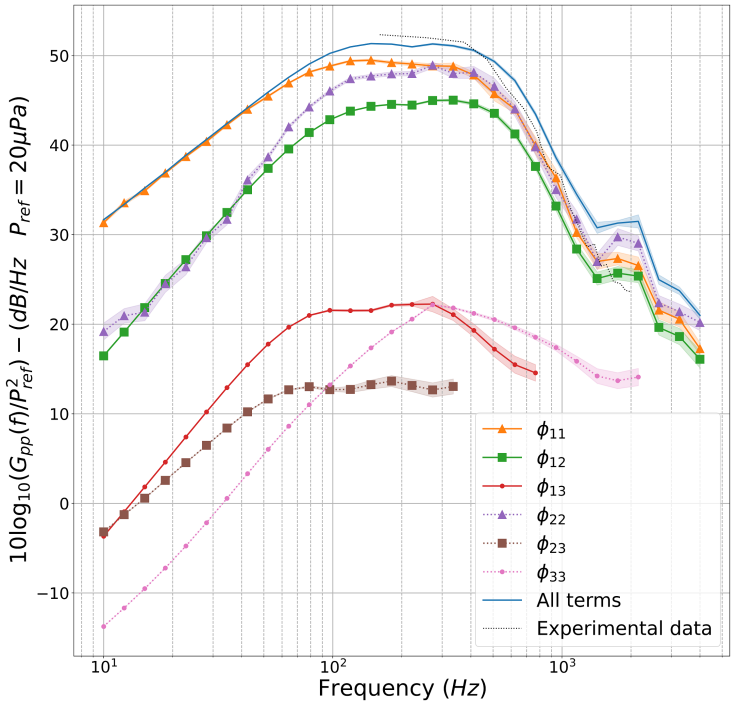

Figure 8: Acoustic pressure spectrum ($G_{pp}(f) = 4\pi S_{pp}(\omega)$) for leading edge noise at an observer at $2.25m$ and at mid-chord above the profile, obtained using Eq. (9) and the compact source approximation of the Green function (A.3). Transparent areas define the estimated integration error given by the VEGAS algorithm.

the turbulence volume in both the streamwise and normal directions have no impact on the radiated noise levels. Therefore we consider a box defined by $\{(y_1, y_2, y_3), y_1 \in [0, c], y_2 \in [-c, c], y_3 \in [-L/2, L/2]\}$. The observer is located at a distance 2.25 m from the mid-chord of the airfoil at $\mathbf{x} = (-0.115, 2.25, 0)$. Four wind speeds are chosen : 40.0 m.s^{-1}, 60.0 m.s^{-1}, 90.0 m.s^{-1} and 120.0 m.s^{-1}. Figure 7 shows the far-field radiated noise spectrum predictions obtained for both the Half Plane and the Multiple Scattering Green function. Predictions appear to be in excellent agreement with experimental data, especially when the Multiple Scattering Green's function is used. Because our model allows us to take into account the effective distance of the eddies to the edge, unlike the surfacic approaches of Amiet or of the diffraction theory, no additional thickness correction term is required for leading edge noise prediction [33].

Figure 8 shows a comparison of the contribution of each term to the leading edge noise for the lowest speed ($M = 0.12$). Each curve shows the result of the calculation of the integral of the Eq. (9) by isolating each term $\widehat{\phi_{ij}}$, i.e. by considering each time that all the $\widehat{\phi_{ij}}$ terms are zero except one. At low frequencies, only the $\widehat{\phi_{11}}$ term has a significant contribution. At 100 Hz and above, $\widehat{\phi_{11}}$ and $\widehat{\phi_{22}}$ are dominant, and at higher frequencies all terms that do not contain the derivative of Green's function in the spanwise direction (i.e., the $\widehat{\phi_{11}}$, $\widehat{\phi_{12}}$, and $\widehat{\phi_{22}}$ terms) have a significant contribution to the radiated noise. The $\widehat{\phi_{13}}$, $\widehat{\phi_{23}}$ and $\widehat{\phi_{33}}$ are not plotted at high frequencies because the convergence of the Monte-Carlo quadrature method failed.

4.3. Boundary layer noise prediction

Boundary layer noise corresponds to the radiation directly associated to the turbulence, in the absence of any diffraction effect. This contribution to the global radiation which necessarily appears when an obstacle is placed in a flow is generally neglected at low Mach number because it can be shown that the ratio between this direct radiation and the radiation related to the diffraction effects is proportional to the Mach number squared. This leads to a lack of quantitative evaluation of the direct radiation in the literature while it is not

clear whether this contribution can be neglected over the whole frequency range. The objective of this section is to present the prediction of this direct radiation for a NACA 0012 airfoil with no incidence angle at $M = 0.06$ and to show, as much as possible, that our predictions are consistent with the empirical models. Since no experimental (or numerical) data are available at such a low Mach number, radiated noise predictions are compared to Howe's model combined with an empirical wall pressure spectral model. First, for an observer above the boundary layer, the far-field radiated pressure spectrum is related to the wavenumber-frequency wall pressure spectrum by [34]:

$$S_{pp}(\mathbf{x}, \omega) = \frac{2\mathcal{A}k_0^2}{|\mathbf{x}|^2} \phi_{pp}\left(0, \omega\right), \tag{18}$$

where $\mathcal{A}$ is the area of the wetted surface. Then, we use three empirical models for the wavenumber-frequency wall pressure spectrum: the Goody's model [35] and the Chase's [7] for a zero pressure gradient flow and the Lee's model [36] that can be used for adverse pressure gradient flows. Goody's model and Lee's model are two models for the one-point wall pressure spectrum and must be used with a model for the wavenumber wall pressure cross-spectrum that can be used in the acoustic wavenumber domain. In the present study, we choose to use these two models with the Smol'yakov and Tkachenko cross-spectrum model [37]. All these empirical wall pressure spectrum models require an estimate of the turbulent boundary layer parameters. However, the location at which they must be computed is arbitrary and, contrary to trailing edge noise predictions, it is not necessarily the sources the closest to the edge that will have the most significant contribution to the radiated noise. Therefore, we extract boundary layer parameters at 75% of the chord ($y_1/c = -0.25$) and at 90% of the chord ($y_1/c = -0.1$). Predictions from Eq. (9) are obtained using the Green function of the half-space :

$$G_T(\mathbf{x}, \mathbf{y}, \omega) = G_0(\mathbf{x}, \mathbf{y}, \omega) + G_0(\mathbf{x}, \mathbf{y}^*, \omega), \tag{19}$$

where $\mathbf{y} = (y_1, y_2, y_3)$ and $\mathbf{y}^* = (y_1, -y_2, y_3)$. The observer is placed as in section 4.1 at $\mathbf{x} = (0.0, 1.22\,\mathrm{m}, 0.0)$ in order to allow a comparison with the observed

levels for the trailing edge noise. An XFoil simulation is used to estimate the evolution of the boundary layer parameters on a NACA 0012 profile of chord $c = 0.2\,\mathrm{m}$ and span $L = 0.45\,\mathrm{m}$ which leads to $\mathcal{A} = 0.09\,\mathrm{m}^2$. At 90% of the chord the friction velocity is equal to $u_\tau = 0.818\,\mathrm{m.s}^{-1}$, the momentum thickness to $\delta^* = 1.125\,\mathrm{mm}$ and the Clauser's parameter to $\beta_c = 4.1$. At 75% of the chord, $u_\tau = 0.926\,\mathrm{m.s}^{-1}$, $\delta^* = 0.834\,\mathrm{mm}$ and $\beta_c = 0.42$. Figure 9 shows a comparison between the predictions obtained from Eq. (9) and the predictions obtained from the empirical wall pressure spectrum models. The configuration being the same as for Figures 2 or 3 (only the Green's function used has been changed), it appears that the levels associated with the contribution of the direct field is more than 25 dB lower than the levels observed for the total field over the whole frequency range. Predictions obtained from Eq. (9) take into account the evolution of the boundary layer along the chord. They appear to be relatively close to the Goody model and the general trend is retrieved. Also, it can be observed on Figure 9 that the Lee results are close to Goody at 75% of the chord but are around 10 dB above Goody's at 90% of the chord where the adverse pressure gradient is more important. We observe that predictions based on Chase's model are close to our predictions above 1000 Hz, which corresponds to $\omega\delta^*/U_\infty > 0.3$. This is expected as the range of validity of the Chase model is rather at high frequencies ($\omega\delta^*/U_\infty > 1$) (See Dowling [7, Figure 16.4]).

4.4. Reducing computational costs

Even if the computational cost is not a main concern in the current study since we use simple analytical Green functions, it may become an issue if we choose to use either the exact Green function (A.1) or a numerical tailored Green function. Our goal here is to try to reduce the computational cost as much as possible. Until now, the calculation of the 6-dimensional integral is performed without taking advantage of the fact that two very distant eddies are perfectly uncorrelated. By introducing r_{max}, a correlation distance beyond which the velocity fluctuations cross-spectrum is considered as equal to zero, it is possible to reduce the computational cost significantly. The simplest approach consists

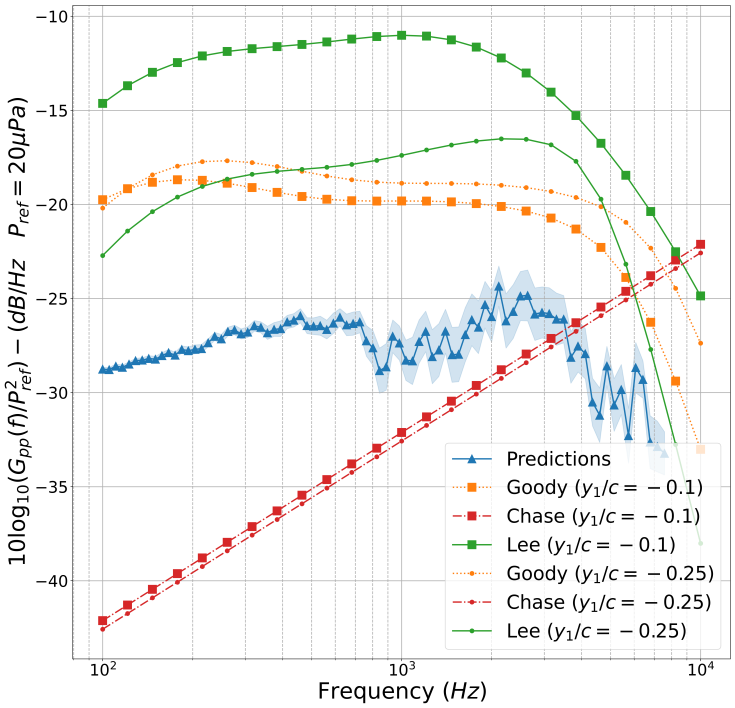

Figure 9: Acoustic pressure spectrum ($G_{pp}(f) = 4\pi S_{pp}(\omega)$) for boundary layer edge noise at an observer at $1.17m$ above the trailing edge obtained using Eq. (9) and the Green function of the half-space (19), and using Goody's and Lee's models combined with the Smol'yakov and Tkachenko model for the wavenumber-frequency wall pressure spectrum. Transparent areas define the estimated integration error given by the VEGAS algorithm.

in using a maximum correlation length that does not depend on the frequency. However, the correct criterion is unknown and requires some computations to be estimated. An alternative is to use a criterion similar to the Corcos' length scales that are inversely proportional to the frequency. We define two different length scales according to the direction. In the streamwise direction, we use $\lambda_1 = 9.0U_\infty/\omega$ and in the spanwise direction $\lambda_3 = 1.4U_\infty/\omega$. Then, by introducing a, a user-defined coefficient, we define a distance criterion $r_{max}^{(i)} = a\lambda_i$ with $i \in \{1, 3\}$. Figure 10 shows the far-field radiated noise spectrum calculations for different values of r_{max}. We consider the same configuration as in Figure 2 at $M = 0.06$. We can observe on the left side of the figure that when the maximum correlation length scale decreases, the predicted levels are good and are mostly comparable, excepting at low frequencies where they tend to decrease with the frequencies. Such a frequency cannot be observed if the frequency-dependent criterion is used. On the right side of the figure, it appears as expected that the predicted levels are underestimated if the parameter a is to small ($a \leq 0.5$). Figure 10 has shown that the results are of course better for a large correlation distance but this is at the cost of a larger computational time. To determine a good compromise between precision and computational costs, the computation times obtained to compute the radiated pressure level for 17 frequencies from 350 Hz to 4500 Hz with the different definitions of r_{max} are given in Table 1. We used a single core i7-10750H CPU@2.60GHz processor for all the computations. It appears that a significant reduction (up to two orders of magnitude) in the required computational time can be obtained with less than 1 dB deviation for $a = 1\,\text{or}\,2$, which seems to be the best compromise. Note that for $a = 1$ the computational time is surprisingly larger than for $a = 2$, but at least leading to a small maximum deviation. The reason is that the computation time is not perfectly controllable since the behavior of the VEGAS algorithm is non-deterministic.

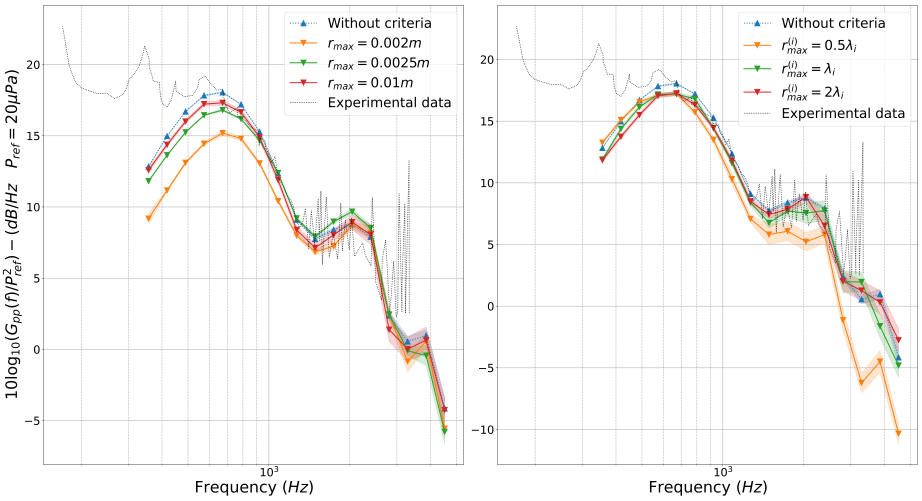

Figure 10: Acoustic pressure spectrum ($G_{pp}(f) = 4\pi S_{pp}(\omega)$) for trailing edge noise at observer at $1.17m$ above the trailing edge obtained using the multiple scattering Green function (A.4). The criteria r_{max} is either defined as a constant (*left*) or from Corcos' length scales (*right*). Transparent areas define the estimated integration error given by the VEGAS algorithm.

Table 1: Impact of r_{max} on the computation time, speedup values and the maximum deviation obtained between 350 Hz and 4500 Hz

Criteria r_{max}	Computation time	Speedup	Maximum deviation
Without criteria	6534 s	1	0
0.01 m	467 s	14	0.74 dB
0.0025 m	178 s	36.7	1.46 dB
0.002 m	66 s	99	3.82 dB
$0.5\lambda_i$	47 s	140	1.79 dB
λ_i	257 s	25.4	0.94 dB
$2\lambda_i$	163 s	40	1.24 dB

5. Conclusion

By using a tailored Green's function and a new analytical model for the statistical description of the turbulent flow, we have developed an approach for flow noise prediction which can be applied to realistic rigid airfoil geometries. This preliminary study aims at proving the validity of the method in term of both computational cost and accuracy. It appears that, even with a quite simple estimate of the boundary layer parameters and an analytical model for the mean velocity, trailing edge noise predictions are in good agreement with experimental data. Using measured values of the integral length scale and of the turbulence intensity, the model is also able to predict accurately the leading edge noise as well without any empirical thickness correction. The main advantage of the approach presented in this study is that it allows us to take into account the true location of the noise sources and to study the relative contributions of the sources inside the volume. In addition, the model can be used to provide an estimation of the boundary layer noise which is usually neglected at low Mach number. The calculation of the 6-dimensional integral appeared to be tractable using an efficient Monte Carlo quadrature algorithm. As shown in Section 4.4, a relatively low CPU time is required when a reasonable limit on the correlation length scale is set.

The approach presented in this study can be extended in various ways. In the sequel of this study, our main objective is to apply this approach to rigid boundaries of arbitrary shapes by using a numerical Green's function. The numerical Green's function, tailored to a given arbitrary geometry, can be determined using a specific Boundary Element Method which has been introduced in [38]. Moreover, the turbulence model introduced in this approach can be used straightforwardly with a simulation of the mean-flow which could handle more complex three-dimensional flows. Finally, it would be interesting to add the contribution of turbulence-turbulence interaction terms, that are neglected in the present study.

Acknowledgements

The authors would like to thank Naval Group and *Association Nationale Recherche et Technologie* (ANRT) for supporting this work.

Appendix A. Analytical tailored Green's function

This appendix aims to present analytical expressions for the tailored Green function that are used in Eq. (9). The exact Green function tailored to the infinite half plane defined by $\{(y_1, y_2, y_3), y_2 = 0, y_1 < 0\}$ and described in Fig. 1 is [39]:

$$\mathrm{G}_T(\mathbf{x},\mathbf{y},\omega) = \frac{-i}{8\pi}\int_{-\infty}^{\infty}\sum_{m=0}^{\infty} a_m \left[\mathrm{J}_{\nu_m}(\gamma r_x)\mathrm{H}^{(1)}_{\nu_m}(\gamma r_y)\mathrm{H}(r_y - r_x) + \mathrm{J}_{\nu_m}(\gamma r_y)\mathrm{H}^{(1)}_{\nu_m}(\gamma r_x)\mathrm{H}(r_x - r_y)\right] \times \cos\left(\nu_m(\theta_x+\pi)\right)\cos\left(\nu_m(\theta_y+\pi)\right)\mathrm{e}^{\mathrm{i}k_3(x_3-y_3)}dk_3, \tag{A.1}$$

where $\gamma = \gamma(k_3) = \sqrt{k_0^2 - k_3^2}$, H is the Heaviside function, J_{ν_m} is the Bessel function of order ν_m, $a_0 = 1$, $a_m = 2$ and where $\mathrm{H}^{(1)}_{\nu_m}$ is the Hankel function of the first kind of order ν_m. Observer and source locations are respectively expressed in cylindrical coordinates by $\mathbf{x} = (r_x, \theta_x, x_3)$ and $\mathbf{y} = (r_y, \theta_y, y_3)$ with $\theta_{x,y} \in (-\pi, \pi)$. In particular, we consider an observer in the far field $r_x \gg r_y$ and then using the asymptotic behavior of the Hankel function and the theorem of the stationary phase, Eq. (A.1) can be reduced to [39]:

$$\mathrm{G}_T(\mathbf{x},\mathbf{y},\omega) \approx -\frac{1}{4\pi}\sum_{m=0}^{\infty} a_m \cos\left(\nu_m(\theta_x+\pi)\right)\cos\left(\nu_m(\theta_y+\pi)\right)\mathrm{J}_{\nu_m}(k_0 r_y \sin A)\frac{\mathrm{e}^{\mathrm{i}k_0|\mathbf{x}-y_3\mathbf{e_3}|}}{|\mathbf{x}-y_3\mathbf{e_3}|}\mathrm{e}^{-\mathrm{i}\pi m/4}, \quad |\mathbf{x}| \to \infty, \tag{A.2}$$

with $\tan A = r_x/(x_3 - y_3)$. Formulations (A.1) and (A.2) are quite expensive to compute especially at high frequencies. This is a problem since if one attempts to compute (1) considering a finite boundary layer over a semi-infinite half plane, the Green function will have to be evaluated at many points and in particular where $k_0 r_y$ is not small which requires to include many terms in the sums of Eqs. (A.1) or (A.2). But as we will detail now, only areas close to the edge

($k_0 r_y \ll 1$) have to be taken into account. Indeed, according to the analysis of Ffowcs Williams and Hall [8] analysis, three regions in the turbulent volume can be distinguished. For a source far from the edge ($k_0 r_y \gg 1$) and located upstream, the tailored Green function (Eq. (A.1)) is equal to the half-space Green function, meaning that $\mathrm{G}_S \approx \mathrm{G}_0$. Therefore, a source upstream and far from the edge will have a contribution of specular nature to the total radiated field. For a source located downstream and far from the edge, the tailored Green function is equal to the free-field Green function, so $\mathrm{G}_S \approx 0$. Finally, for a source located near the edge ($k_0 r_y \ll 1$) the classic cardioid directivity patern is recovered, meaning that the scattered part of the tailored Green function is dominant ($\mathrm{G}_S \gg \mathrm{G}_0$). Thus, we expect that sources in the vicinity of the edge will have the highest contribution to the total radiated field.

In the numerical tests, an approximation of Eq. (A.2) will by used. Indeed, close to the edge, Eq. (A.2) can be further simplified. Restricting the sum in (A.2) to $m \leq 1$ and considering $k_0 r_y \ll 1$ lead to the so-called compact Green function used in the theory of Howe [3]:

$$\mathrm{G}_T(\mathbf{x},\mathbf{y},\omega) = \frac{-\mathrm{e}^{\mathrm{i}k_0|\mathbf{x}-y_3\mathbf{e_3}|}}{4\pi|\mathbf{x}-y_3\mathbf{e_3}|} - \frac{\sqrt{k_0 r_x}\sin(\theta_x/2)\sqrt{r_y}\sin(\theta_y/2)}{\pi\sqrt{2\mathrm{i}\pi}|\mathbf{x}-y_3\mathbf{e_3}|^{3/2}}\mathrm{e}^{\mathrm{i}k_0|\mathbf{x}-y_3\mathbf{e_3}|}, \quad k_0 r_y \ll 1, \quad |\mathbf{x}| \to \infty, \tag{A.3}$$

It is important to notice that, unlike the Howe's theory that is expressed in the Fourier space and thus considers an infinite spatial extent of the boundary layer in the streamwise direction, the approach presented here takes into account the true shape of the turbulent boundary layer for which the compact source approximation of the Green function may not be suitable. Indeed, there are less and less eddies *close to the edge* (i.e. satisfying $k_0 r_y \ll 1$) when we increase the frequency and therefore the contribution of an increasing number of eddies will be poorly predicted. In order to investigate this aspect, we show in Figs. A.11 and A.12 two comparisons between Eqs. (A.2) and (A.3). In both cases, the observer is located in the far-field above the trailing edge and the absolute value of the Green function, respectively the absolute value of the second derivatives of the Green function, is plotted versus the location of a source around the half

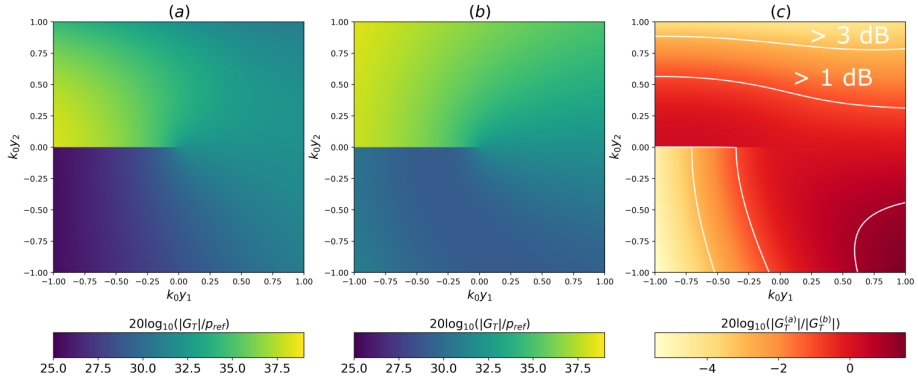

Figure A.11: Exact Green's function tailored to the semi-infinite plate $\{(y_1, y_2, y_3), y_2 = 0, y_1 < 0\}$ computed (a), with Eq. (A.2) or (b), with Eq. (A.3). The observation point is set far above the edge at $\mathbf{x} = (0.0, 100.0\text{m}, 0.0)$ and the frequency to $k_0 = 1\ \text{m}^{-1}$. (c) is the relative error due to the compact source approximation.

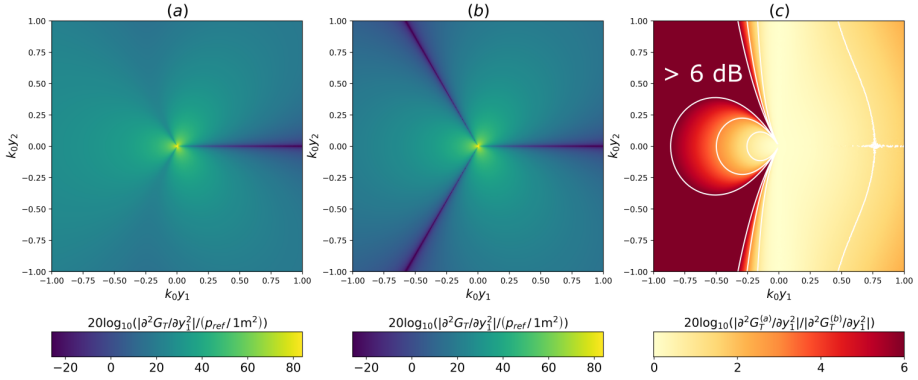

Figure A.12: Second derivative of the exact Green's function tailored to the semi-infinite plate $\{(y_1, y_2, y_3), y_2 = 0, y_1 < 0\}$ corresponding to the radiation of a longitudinal quadrupole, computed (a), with Eq. (A.2) or (b), with Eq. (A.3) and (c) the relative error between both. The observation point is set far above the edge at $\mathbf{x} = (0.0, 100.0\text{m}, 0.0)$ and the frequency to $k_0 = 1\ \text{m}^{-1}$. The relative error due to the compact source approximation (c) is caped at 100%.

plane edge. The coordinate system is the same as the one defined in Fig. 1. It appears that the compact Green's function deviates faster from the approximated Green's function on the lighted side ($k_0 y_1 < 0; k_0 y_2 > 0$) than on the shadow side ($k_0 y_1 < 0; k_0 y_2 < 0$). Obviously Eq. (A.3) is mostly a poor approximation of Eq. (A.2) except when $k_0|\mathbf{y}| \ll 1$ as expected. But it is not the case for the second derivatives of G. Indeed, Fig. A.12 shows that the second derivatives values are maximum for sources very close to the edge precisely in areas where the compact approximation is accurate. Thus, these sources have a significant contribution on the radiated noise, and formulation (A.3) is expected to be a good approximation. An extension of Eq. (A.3) for a plate of finite chord exists: it is the Multiple Scattering Green function derived by Howe [40] that can be used to take into account the back-scattering by opposite edges:

$$\mathrm{G}_T(\mathbf{x},\mathbf{y},\omega) = \mathrm{G}_{HP}(\mathbf{x},\mathbf{y},\omega) + \mathrm{G}_{LE}(\mathbf{x},\mathbf{y},\omega) + \mathrm{G}_{TE}(\mathbf{x},\mathbf{y},\omega), \tag{A.4}$$

where,

$$\begin{cases} \mathrm{G}_{LE} &= \dfrac{\sqrt{k_0 \sin\psi_x}\varphi^*(\mathbf{y})\mathrm{e}^{\mathrm{i}k_0(|\mathbf{x}'|+c\sin\psi_x)}}{\mathrm{i}\pi^{3/2}|\mathbf{x}|(1+\mathrm{e}^{2\mathrm{i}k_0 c\sin\psi_x}/2\pi\mathrm{i}k_0 c\sin\psi_x)}\mathcal{F}\left(2\sqrt{\dfrac{k_0 c\sin\psi_x\cos^2(\theta_x/2)}{\pi}}\right) \\ \mathrm{G}_{TE} &= \dfrac{-\varphi^*(\mathbf{y})\mathrm{e}^{\mathrm{i}k_0(|\mathbf{x}|+2c\sin\psi_x)}}{\pi^2\sqrt{2\mathrm{i}c}|\mathbf{x}|(1+\mathrm{e}^{2ik_0 c\sin\psi_x}/2\pi i k_0 c\sin\psi_x)}\mathcal{F}\left(2\sqrt{\dfrac{k_0 c\sin\psi_x\sin^2(\theta_x/2)}{\pi}}\right) \\ \mathcal{F}(x) &= \dfrac{1}{2+4.142x+3.492x^2+6.670x^3} + \mathrm{i}\dfrac{1+0.926x}{2+1.792x+3.104x^2} \end{cases},$$

with $\varphi^*(\mathbf{y}) = \sqrt{r_y}\sin(\theta_y/2)$ and where G_{HP} (*Half Plane*) is the Green function tailored to the semi-infinite plate given by Eq. (A.3). This Green function appears to be suitable for the prediction of both the trailing edge [18] and leading edge [33] noise radiated by a NACA 0012 airfoil.

Appendix B. Calculation of the turbulent parameters from an estimation of the boundary layer parameters

This appendix presents how it is possible to calculate the input parameters needed to compute Equation 16 from an estimate of the boundary layer

parameters. First of all, the boundary layer thickness can be expressed as [31]:

$$\delta_{bl} = \theta \left(3.14 + \frac{1.72}{\frac{\delta^*}{\theta} - 1} \right) + \delta^*. \tag{B.1}$$

The mean velocity profile is chosen to be calculated with the Cole's log-wake empirical law [41]:

$$U_1(y_1, y_2) = u_\tau(y_1) \left[\frac{1}{\kappa} \ln \left(\frac{u_\tau(y_1) y_2}{\nu} \right) + B + W \left(\frac{y_2}{\delta_{bl}} \right) \right], \tag{B.2}$$

with $\kappa = 0.41$ the von Kármán constant, $B = 5.5$ an additive empirical constant and u_τ the friction velocity. The latter can be obtained from the friction coefficient C_f:

$$u_\tau(y_1) = \sqrt{\frac{1}{2} C_f(y_1) U_e(y_1)^2}. \tag{B.3}$$

The wake function $W\left(y_2/\delta_{bl}\right)$ takes into account the effect of a pressure gradient on the mean velocity. It can be related analytically to the local pressure gradient [42] but this can lead to a bad estimate of the velocity near the boundary layer edge. Another approach, which appears to yield to better results when a good estimate of the local pressure gradient is not available, consists in forcing the velocity at the boundary layer edge. Following [42], we start by assuming that the wake function is in the form:

$$W \left(\frac{y_2}{\delta_{bl}} \right) = \frac{2\Pi_w}{\kappa} \sin^2 \left(\frac{\pi y_2}{2\delta_{bl}} \right), \tag{B.4}$$

where Π_w is the Cole's wake parameter. Then, the strategy is to consider that the pressure gradient Π_w depends on y_1 and to adjust it in order to get the correct velocity at the boundary layer edge. Finally imposing the condition $U_1(y_1, y_2 = \delta_{bl}) = U_e(y_1)$ yields [18]:

$$W \left(\frac{y_2}{\delta_{bl}} \right) = \sin^2 \left(\frac{\pi y_2}{2\delta_{bl}} \right) \left(\frac{U_e(y_1)}{u_\tau(y_1)} - \frac{1}{\kappa} \ln \left(\frac{u_\tau(y_1)\delta_{bl}}{\nu} \right) - B \right). \tag{B.5}$$

It is then expected to fit experimental results very accurately near the boundary layer edge. Furthermore, the longitudinal integral length scale is related to the vertical integral length scale [19] by:

$$2L_{22}^{(2)} = L_{11}^{(1)}. \tag{B.6}$$

The vertical integral length scale can be built from the Prandt's mixing length scale l_m, that can be expressed as a function of the distance to the wall by [43]:

$$L_{22}^{(2)} = \frac{l_m}{\kappa} \quad \text{with} \quad l_m = \frac{0.085\delta_{bl}\tanh\left(\frac{\kappa y_2}{0.085\delta_{bl}}\right)}{\sqrt{\left(1+B\frac{y_2}{\delta_{bl}}\right)^6}}. \tag{B.7}$$

Prandt's mixing length scale hypothesis assumes that the turbulent kinetic energy is related to the mixing length scale and to the local mean shear by [18]:

$$k_T = \sqrt{l_m^4\left(\frac{\partial U_1}{\partial y_2}\right)^4/C_\mu}, \tag{B.8}$$

where $C_\mu = 0.09$. The variance of the turbulence fluctuations can then be related to the turbulent kinetic energy with:

$$\overline{u^2} = \alpha k_T, \tag{B.9}$$

where α is an empirical parameter equal to 0.45 for a symmetric airfoil with zero angle of attack. Because the boundary layer parameters depend on the source coordinate in the streamwise direction (y_1), and the mixing length scale depends on the source coordinate in the vertical direction (y_2), the integral length scale and the mean flow velocity must depend on the position of both sources $\mathbf{y}$ and $\mathbf{z}$ and we must introduce an inhomogeneity in the model. Therefore, we assume following [10], that the vertical integral length scale can be approximated as:

$$L_{22}^{(2)}(\mathbf{y},\mathbf{z}) = \sqrt{L_{22}^{(2)}(\mathbf{y})L_{22}^{(2)}(\mathbf{z})}, \tag{B.10}$$

and that the convection mean velocity can be expressed as the local mean velocity:

$$U_c(\mathbf{y},\mathbf{z}) = \frac{U_1(\mathbf{y})+U_1(\mathbf{z})}{2}. \tag{B.11}$$

Similarly the turbulent kinetic energy, which is related to the mixing length scale, is computed using the geometric mean:

$$k_T(\mathbf{y},\mathbf{z}) = \sqrt{k_T(\mathbf{y})k_T(\mathbf{z})}. \tag{B.12}$$

Appendix C. Derivation of the expression for the turbulent velocity cross-correlation spectrum

This Appendix aims to present the analytical calculation of the inverse Fourier transform (15). Introducing the von Kármán model for the turbulent kinetic energy spectrum (11) in (10) yields:

$$\widetilde{\phi_{ij}}^{(1,2,3)}(k_1,k_2,k_3) = \frac{55}{9\sqrt{\pi}}\frac{\Gamma(5/6)}{\Gamma(1/3)}\frac{1}{4\pi}\frac{\overline{u^2}}{k_{\mathrm{e}}^3}\widetilde{F_{ij}}(k_1,k_2,k_3), \tag{C.1}$$

with

$$\widetilde{F_{ij}}(k_1,k_2,k_3) = \frac{(k/k_e)^2\delta_{ij} - (k_ik_j/k_{\mathrm{e}}^2)}{[1+(k/k_e)^2]^{(17/6)}}. \tag{C.2}$$

Therefore (15) can be expressed in the physical space by:

$$\begin{aligned}\phi_{ij}(r_1,r_2,r_3,\omega) &= \frac{55}{9\sqrt{\pi}}\frac{\Gamma(5/6)}{\Gamma(1/3)}\frac{1}{4\pi}\frac{\overline{u^2}}{k_{\mathrm{e}}^3}\mathrm{e}^{-\gamma|\omega r_1/U_c|}\frac{\mathrm{e}^{\mathrm{i}\omega r_1/U_c}}{U_c}\iint_{-\infty}^{\infty}\widetilde{F_{ij}}(k_1,k_2,k_3)\mathrm{e}^{\mathrm{i}k_m r_m}d^2k_m \\ &= \frac{55}{9\sqrt{\pi}}\frac{\Gamma(5/6)}{\Gamma(1/3)}\frac{1}{4\pi}\frac{\overline{u^2}}{k_{\mathrm{e}}^3}\mathrm{e}^{-\gamma|\omega r_1/U_c|}\frac{\mathrm{e}^{\mathrm{i}\omega r_1/U_c}}{U_c}\iint_{-\infty}^{\infty}k_{\mathrm{e}}^2\frac{(q_1^2+q^2)\delta_{ij}-q_iq_j}{(1+q_1^2+q^2)^{(17/6)}}\mathrm{e}^{\mathrm{i}k_e q_m r_m}d^2q_m,\end{aligned} \tag{C.3}$$

with $q_m = k_m/k_e$ for $m \in \{2,3\}$, $q_1 = \omega/(k_eU_c)$ and $q^2 = q_2^2+q_3^2$. The integral in (C.3) can be computed analytically. Introducing ([44], example 2.2, p.106):

$$h_l(\xi_2,\xi_3,\omega) = \iint_{-\infty}^{\infty}\frac{\mathrm{e}^{\mathrm{i}q_m\xi_m}}{(c+q^2)^l}dq_m = 2\pi\frac{2^{1-l}}{\Gamma(l)}\left(\sqrt{\frac{\xi_2^2+\xi_3^2}{c}}\right)^{l-1}\mathrm{K}_{l-1}\left(\sqrt{c(\xi_2^2+\xi_3^2)}\right), \tag{C.4}$$

where $c = 1+(\omega/k_eU_c)^2$, where $l = 17/6$ and K is a Bessel of second kind, it can be observed that for $i = 2$ or 3:

$$\frac{\partial h_l}{\partial \xi_i} = \iint_{-\infty}^{\infty}\frac{\mathrm{i}q_i}{(c+q_m^2)^l}\mathrm{e}^{\mathrm{i}q_m\xi_m}dq_m. \tag{C.5}$$

It appears that we can express ϕ_{ij} with respect to q_i, h_l and its derivatives. Finally, the expression for the turbulent velocity cross-correlation spectrum, assuming an isotropic and homogeneous turbulence, Eq. (16), is recovered:

$$\phi_{ij}(r_1,r_2,r_3,\omega) = \frac{55}{9\sqrt{\pi}}\frac{\Gamma(5/6)}{\Gamma(1/3)}\frac{\overline{u^2}}{4\pi k_e}\mathrm{e}^{-\gamma|\omega r_1/U_c|}\frac{\mathrm{e}^{\mathrm{i}\omega r_1/U_c}}{U_c}\varphi_{ij}(\xi_2,\xi_3,\omega), \tag{C.6}$$

where $\xi_i = k_e r_i$ and with:

$$\varphi_{11}(\xi_2,\xi_3,\omega) = h_{l-1}(\xi_2,\xi_3,\omega) - c \times h_l(\xi_2,\xi_3,\omega), \tag{C.7}$$

$$\varphi_{22}(\xi_2,\xi_3,\omega) = q_1^2 h_l(\xi_2,\xi_3,\omega) - \frac{\partial^2 h_l}{\partial \xi_3^2}(\xi_2,\xi_3,\omega), \tag{C.8}$$

$$\varphi_{33}(\xi_2,\xi_3,\omega) = q_1^2 h_l(\xi_2,\xi_3,\omega) - \frac{\partial^2 h_l}{\partial \xi_2^2}(\xi_2,\xi_3,\omega), \tag{C.9}$$

$$\varphi_{12}(\xi_2,\xi_3,\omega) = \varphi_{21}(\xi_2,\xi_3,\omega) = iq_1 \frac{\partial h_l}{\partial \xi_2}(\xi_2,\xi_3,\omega), \tag{C.10}$$

$$\varphi_{13}(\xi_2,\xi_3,\omega) = \varphi_{31}(\xi_2,\xi_3,\omega) = iq_1 \frac{\partial h_l}{\partial \xi_3}(\xi_2,\xi_3,\omega), \tag{C.11}$$

$$\varphi_{23}(\xi_2,\xi_3,\omega) = \varphi_{32}(\xi_2,\xi_3,\omega) = \frac{\partial^2 h_l}{\partial \xi_2 \partial \xi_3}(\xi_2,\xi_3,\omega). \tag{C.12}$$

$$\tag{C.13}$$

References

[1] J. Lighthill, On sound generated aerodynamically. i. general theory, Proceedings of The Royal Society A: Mathematical, Physical and Engineering Sciences 211 (1952) 564–587. doi:10.1098/rspa.1952.0060.

[2] N. Curle, The influence of solid boundaries upon aerodynamic sound, Proceedings of The Royal Society A: Mathematical, Physical and Engineering Sciences 231 (1955) 505–514. doi:10.1098/rspa.1955.0191.

[3] M. Howe, Trailing edge noise at low Mach numbers, Journal of Sound and Vibrationdoi:10.1006/jsvi.1999.2236.

[4] C. Schram, J. Anthoine, A. Hirschberg, Calculation of sound scattering using Curle's analogy for non-compact bodies, in: 11th AIAA/CEAS Aeroacoustics Conference (26th AIAA Aeroacoustics Conference), American Institute of Aeronautics and Astronautics, 2005. doi:10.2514/6.2005-2836.

[5] C. Bogey, C. Bailly, D. Juvé, Computation of flow noise using source terms in linearized Euler's equations, AIAA Journal 40 (2002) 235–243. doi:10.2514/3.15055.

[6] C. Schram, A boundary element extension of Curle's analogy for non-compact geometries at low-Mach numbers, Journal of Sound and Vibration 322 (2009) 264–281. doi:10.1016/j.jsv.2008.11.011.

[7] D. Crighton, A. Dowling, J. Ffowcs Williams, M. Heckl, F. Leppington, Modern Methods In Analytical Acoustics, Springer-Verlag London, 1992.

[8] J. Ffowcs Williams, L. Hall, Aerodynamic sound generation by turbulent flow in the vicinity of a scattering half plane, Journal of Fluid Mechanics 40 (4). doi:10.1017/S0022112070000368.

[9] W. Devenport, N. Alexander, S. Glegg, M. Wang, The sound of flow over rigid walls, Annu. Rev. Fluid Mech. 50 (2018) 435–458. doi:10.1146/annurev-fluid-122316-045056.

[10] A. Fischer, F. Bertagnolio, H. A. Madsen, Improvement of TNO type trailing edge noise models, European Journal of Mechanics - B/Fluids 61 (2017) 255 – 262, rotating Flows. doi:10.1016/j.euromechflu.2016.09.005.

[11] T. Takaishi, M. Miyazawa, C. Kato, A computational method of evaluating noncompact sound based on vortex sound theory, The Journal of the Acoustical Society of America 121 (3) (2007) 1353–1361. doi:10.1121/1.2431345.

[12] S. Lee, L. Ayton, F. Bertagnolio, S. Moreau, T. Chong, P. Joseph, Turbulent boundary layer trailing-edge noise: Theory, computation, experiment, and application, Progress in Aerospace Sciences 126. doi:10.1016/j.paerosci.2021.100737.

[13] R. Amiet, Noise due to turbulent flow past a trailing edge, Journal of Sound and Vibration 47 (3) (1976) 387 – 393. doi:10.1016/0022-460X(76)90948-2.

[14] D. M. Chase, Sound radiated by turbulent flow off a rigid half-plane as obtained from a wavevector spectrum of hydrodynamic pressure, The Journal of the Acoustical Society of America 52 (3B) (1972) 1011. doi:10.1121/1.1913170.

[15] K. L. Chandiramani, Diffraction of evanescent waves, with applications to aerodynamically scattered sound and radiation from unbaffled plates, The Journal of the Acoustical Society of America 55 (1) (1974) 19–29. doi:10.1121/1.1919471.

[16] G. Grasso, P. Jaiswal, H. Wu, S. Moreau, M. Roger, Analytical models of the wall-pressure spectrum under a turbulent boundary layer with adverse pressure gradient, Journal of Fluid Mechanics 877 (2019) 1007–1062. doi:10.1017/jfm.2019.616.

[17] S. Moreau, M. Roger, Back-scattering correction and further extensions of

Amiet's trailing-edge noise model. Part II: Application, Journal of Sound and Vibration 323 (2009) 397–425.

[18] S. Lee, Source characterization of turbulent boundary layer trailing edge noise using an improved TNO model, in: 22nd AIAA/CEAS Aeroacoustics Conference (37th AIAA Aeroacoustics Conference), American Institute of Aeronautics and Astronautics, 2016.

[19] O. Stalnov, C. Paruchuri, P. Joseph, Towards a non-empirical trailing edge noise prediction model, Journal of Sound and Vibration 372. doi:10.1016/j.jsv.2015.10.011.

[20] M. Herr, R. Ewert, C. Rautmann, M. Kamruzzaman, D. Bekiropoulos, A. Iob, R. Arina, P. Batten, S. Chakravarthy, F. Bertagnolio, Broadband trailing-edge noise predictions—overview of banc-iii results, 21st AIAA/CEAS Aeroacoustics ConferencearXiv:https://arc.aiaa.org/doi/pdf/10.2514/6.2015-2847, doi:10.2514/6.2015-2847.
URL https://arc.aiaa.org/doi/abs/10.2514/6.2015-2847

[21] S. Glegg, W. Devenport, Aeroacoustics of low Mach number flows: Fundamentals, analysis, and measurement, Academic Press, 2017.

[22] X. Gloerfelt, Flow-induced cylinder noise formulated as a diffraction problem for low Mach numbers, Journal of Sound and Vibration 287 (1) (2005) 129–151. doi:10.1016/j.jsv.2004.10.047.

[23] Y. Khalighi, A. Mani, F. Ham, P. Moin, Prediction of sound generated by complex flows at low Mach numbers, AIAA Journal 48 (2010) 306–316. doi:10.2514/1.42583.

[24] J. Ffowcs Williams, The theoretical modelling of aerodynamic noise, Proceedings of the Indian Academy of Sciences Section C: Engineering Sciences 1 (1) (1978) 57–72.

[25] J. Christophe, J. Anthoine, S. Moreau, Trailing edge noise of a controlled-diffusion airfoil at moderate and high angle of attack, in: 15th AIAA/CEAS

Aeroacoustics Conference (30th AIAA Aeroacoustics Conference), American Institute of Aeronautics and Astronautics, 2009. doi:10.2514/6.2009-3196.

[26] R. Ewert, C. Appel, J. Dierke, M. Herr, RANS/CAA based prediction of NACA 0012 broadband trailing edge noise and experimental validation, 15th AIAA/CEAS Aeroacoustics Conference (30th AIAA Aeroacoustics Conference)doi:10.2514/6.2009-3269.

[27] R. L. Panton, J. H. Linebarger, Wall pressure spectra calculations for equilibrium boundary layers, Journal of Fluid Mechanics 65 (2) (1974) 261–287. doi:10.1017/S0022112074001388.

[28] W. H. Press, S. A. Teukolsky, W. T. Vetterling, B. P. Flannery, Numerical Recipes 3rd Edition: The Art of Scientific Computing, 3rd Edition, Cambridge University Press, USA, 2007.

[29] P. G. Lepage, A new algorithm for adaptive multidimensional integration, Journal of Computational Physics 27 (2) (1978) 192 – 203. doi:10.1016/0021-9991(78)90004-9.

[30] W. Blake, Mechanics of flow-induced sound and vibration, Vol. I and II, in Applied Mathematics and Mechanics, Academic press, 1986.

[31] M. Drela, XFOIL: An Analysis and Design System for Low Reynolds Number Airfoils (1989).

[32] R. W. Paterson, R. K. Amiet, Noise and surface pressure response of an airfoil to incident turbulence, Journal of Aircraft 14 (8) (1977) 729–736. doi:10.2514/3.58845.

[33] J. Gershfeld, Leading edge noise from thick foils in turbulent flows, The Journal of the Acoustical Society of America 116 (3) (2004) 1416–1426. doi:10.1121/1.1780575.

[34] M. Howe, Acoustics of fluid-structure interaction, Cambridge university press, 1998.

[35] M. Goody, Empirical spectral model of surface pressure fluctuations, AIAA Journal 42 (9) (2004) 1788–1794. doi:10.2514/1.9433.

[36] S. Lee, Empirical wall-pressure spectral modeling for zero and adverse pressure gradient flows, AIAA Journal 56 (5) (2018) 1818–1829.

[37] A. V. Smol'yakov, V. M. Tkachenko, J. S. Wood, Models of a field of pseudoacoustic turbulent wall pressures and experimental data, Soviet physics. Acoustics 37 (1991) 1199–1207.

[38] S. Chaillat, B. Cotté, J.-F. Mercier, G. Serre, N. Trafny, Efficient evaluation of three-dimensional Helmholtz Green's functions tailored to arbitrary rigid geometries for flow noise simulations, Journal of Computational Physics 452 (2022) 110915. doi:https://doi.org/10.1016/j.jcp.2021.110915. URL https://www.sciencedirect.com/science/article/pii/S002199912100810X

[39] J. Mathews, Mathematical modelling of noise generation in turbofan aeroengines using Green's functions, Ph.D. thesis, University of Cambridge (July 2016).

[40] M. Howe, Edge-source acoustic Green's function for an airfoil of arbitrary chord, with application to trailing edge noise, Jl Mech. Appl. Mathdoi:10.1093/qjmam/54.1.139.

[41] D. Coles, The law of the wake in the turbulent boundary layer, Journal of Fluid Mechanics 1 (2) (1956) 191–226. doi:10.1017/S0022112056000135.

[42] J. Hinze, Turbulence, McGraw-Hill classic textbook reissue series, McGraw-Hill, 1975.
URL https://books.google.fr/books?id=xfRQAAAAMAAJ

[43] M. Kamruzzaman, A. Herrig, T. Lutz, W. Würz, E. Krämer, S. Wagner, Comprehensive evaluation and assessment of trailing edge noise prediction based on dedicated measurements, Noise Control Engineering Journal 59 (2011) 54–67. doi:10.3397/1.3531794.

[44] N. Ortner, P. Wagner, A survey on explicit representation formulae for fundamental solutions of linear partial differential operators, Acta Applicandae Mathematicae 47 (1997) 101–124.